The infrared spectrum of ortho-enstatite from reflectance experiments and first-principle simulations

(Article begins on next page)

04 September 2024

The infrared spectrum of ortho-enstatite from reflectance experiments and first-principle simulations

Raffaella Demichelis,[1]★ Hiroshi Suto,[2] Yves Noël,[3] Hisato Sogawa,[4]† Takahiro Naoi,[2] Chiyoe Koike,[5] Hiroki Chihara,[5] Norimasa Shimobayashi,[6] Matteo Ferrabone[7] and Roberto Dovesi[7]

[1]*Department of Chemistry, Nanochemistry Research Institute, Curtin University, GPO Box U1987, Perth, WA 6845, Australia*
[2]*National Astronomical Observatory of Japan, Osawa 2-21-1, Mitaka, Tokyo 181-8588, Japan*
[3]*ISTEP, UMR 7193, UPMC, CNRS Université Pierre et Marie Curie, Sorbonne Universités, 4 place Jussieu, 75252 Paris, Cedex 05, France*
[4]*Part-time Lecturer, Department of General Education, Faculty of Engineering, Osaka Institute of Technology, Omiya, Asahi-ku, Osaka 535-8585, Japan*
[5]*Department of Earth and Space Science, Osaka University, 1-1 Machikaneyama, Toyonaka, Osaka 560-0043, Japan*
[6]*Department of Geology and Mineralogy, Kyoto University Kitashirakawa Oiwakecho, Sakyo-ku, Kyoto 606-8502, Japan*
[7]*Dipartimento di Chimica IFM, Università degli Studi di Torino and NIS (Nanostructured Interfaces and Surfaces) – Centre of Excellence, Via P. Giuria 7, 10125 Torino, Italy*

ABSTRACT

Infrared (IR) spectra provide a rich amount of information concerning chemical composition, lattice structure, size and shape of circumstellar dust. Accurate reference data are then required for the analysis of the various detected components. This study provides the IR characterization of one of the most frequently observed compounds, $MgSiO_3$ ortho-enstatite, and shows that IR experiments and ab initio techniques can be used synergically to obtain high-quality data concerning crystalline materials. The IR reflectance spectrum of synthetic ortho-enstatite was collected and compared to ab initio results (Gaussian-type basis set, PBE0 hybrid density functional theory (DFT) functional). An excellent agreement is observed both for vibrational frequencies (ν) and intensities, the latter estimated through the oscillator strength. The mean absolute difference between experimental and calculated ν is of the order of 7–8 cm^{-1} (43 out of 65 peaks differ by less than 10 cm^{-1}, only four peaks differ by 15–19 cm^{-1}). The static dielectric tensor and its components (electronic and ionic contributions) were measured and compared to calculated data: differences are in the 2–5 per cent range.

Key words: techniques: miscellaneous – astronomical data bases: miscellaneous – circumstellar matter.

1 INTRODUCTION

Silicates have been recognized as major components of interstellar and circumstellar dust. Their presence was detected by the *Infrared Space Observatory* launched in 1995, and since then these materials have been actively investigated in Solar system, Galactic and extragalactic bodies, with infrared (IR) instruments on ground-based telescopes and space observatories (Wooden, Woodward & Harker 2004; Spoon et al. 2006; Olofsson et al. 2009).

Enstatite ($MgSiO_3$) features are those most frequently detected in IR spectra of dust. This compound can thus represent an important tracer of material transportation and temperature distribution in the observed environments. For this reason, accurate optical data

of enstatite are required, as they would provide extremely useful references for the spectral analysis of astronomic dust.

In this work, the ortho-enstatite IR spectrum was generated with two different independent methods. First, the IR reflectance spectrum of synthetic ortho-enstatite was collected in the range 100–2000 cm^{-1} by using the Japanese IR beamline of the synchrotron radiation facility SPring8. The resulting data are extremely accurate. Secondly, a fully ab initio quantum mechanical calculation was performed, by using all-electron basis sets and the hybrid PBE0 functional. These two schemes turn out to be complementary. Ab initio methods are known to be affected by limits related to the use of approximated Hamiltonians and finite basis sets. On the other hand, they are able to provide the full IR spectrum, including those modes that, although symmetry allowed, are associated with low intensities and then hardly detected or not fully characterized in the experiments (Noël et al. 2006; Balan et al. 2008; Demichelis et al. 2010a). The simulated reflection spectrum is compared to that directly measured on the sample.

★E-mail: raffaella@ivec.org
†Part-time lecturer.

To the authors' knowledge this is the first time that highly accurate experiments and calculations are applied at the same time for the study of the vibrational properties of a complex system as ortho-enstatite.

This paper is structured as follows. Sections 2 and 3 deal with the adopted computational and experimental methods, respectively; in Section 4 results are reported and commented; Section 5 presents the main conclusions.

2 COMPUTATIONAL METHODS

Calculations were performed with the CRYSTAL09 periodic ab initio code (Dovesi et al. 2009). All-electron Gaussian-type basis sets, already used by Noël et al. (2006) and Demichelis et al. (2010a) in previous works on α-MgSiO$_4$ forsterite (Mg: 85-11G*; Si: 86-311G*; O: 8-411G*) and the hybrid PBE0 (Adamo & Barone 1999) functional, were adopted. Hybrid Hartree–Fock (HF)/DFT schemes were recently shown to provide excellent results for geometry and vibrational frequencies of forsterite (Demichelis et al. 2010a), superior to those obtained with Local Density or Generalised Gradient approximations.

The level of accuracy in evaluating the Coulomb and Hartree–Fock exchange series is controlled by five parameters (Pisani et al. 2000; Dovesi et al. 2009) for which the values 7, 7, 7, 7 and 14 were used. The threshold on the Self Consistent Field energy was set to $10^{-8} E_h$ for the geometry optimization and $10^{-10} E_h$ for the frequency calculation. The reciprocal space was sampled according to a sublattice with shrinking factors (Dovesi et al. 2009) 3 (along the a lattice parameter) and 4 (b and c), corresponding to 18 independent k vectors in the irreducible part of the Brillouin zone.

The DFT exchange-correlation contribution is evaluated by numerical integration over the unit cell volume. In CRYSTAL, radial and angular points of the grid are generated through Gauss–Legendre radial quadrature and Lebedev two-dimensional angular point distributions. A (75, 974)-point grid was used, corresponding to a pruned grid with 75 radial and 974 angular points. The accuracy in the integration can be estimated by the error of the integrated electronic charge density in the unit cell ($\Delta_e = 5.3 \times 10^{-5} |e|$ on a total of 800 electrons).

The structure was optimized by using the analytical energy gradients with respect to atomic coordinates and unit cell parameters (Civalleri et al. 2001; Doll 2001; Doll, Harrison & Saunders 2001) within a quasi-Newton scheme combined with the Broyden–Fletcher–Goldfarb–Shanno algorithm for Hessian updating (Broyden 1970; Fletcher 1970; Goldfarb 1970; Shanno 1970). Convergence was checked on both gradient components and nuclear displacements, for which the default values (Dovesi et al. 2009) were chosen. The vibrational frequencies were obtained by diagonalizing the dynamical matrix, computed by differentiating numerically the analytical gradient of the total energy with respect to atomic Cartesian coordinates. Details on the calculation of harmonic vibrational frequencies can be found in Pascale et al. (2004).

The diagonal j components of the oscillator strength tensor (off-diagonal terms are null in orthorhombic systems) of the nth mode, $f_{n,j}$, are defined as

$$f_{n,j} = \frac{4\pi}{V} \frac{\bar{Z}_{n,j}^2}{v_n^2}, \tag{1}$$

where V is the unit cell volume, j indicates the Cartesian components, v_n is the frequency of the nth mode. $Z_{n,j}$ is the mode effective charge vector, i.e. the projection of the Born atomic effective charge matrix associated with the atom A, $Z_{A,jl}^*$, on the eigenvector of the

mass-weighted Hessian matrix, $t_{n,Al}$ (Zicovich-Wilson et al. 2008):

$$\bar{Z}_{n,j} = \sum_{A,l} t_{n,Al} Z_{A,jl}^* \frac{1}{\sqrt{M_A}}, \tag{2}$$

where M_A is the atomic mass. The Born atomic effective charge matrix elements are defined as the first derivatives of the dipole moments along the j direction, μ_j, with respect to the displacement of atom A along the l direction, u_{Al}:

$$Z_{A,jl}^* = \frac{\partial \mu_j}{\partial u_{Al}} \tag{3}$$

and are evaluated through well-localized Wannier functions (Baranek et al. 2001; Zicovich-Wilson, Dovesi & Saunders 2001; Noël et al. 2002; Zicovich-Wilson et al. 2002).

The intensity I_n of IR vibrational mode v_n is a scalar quantity related to the oscillator strengths (Zicovich-Wilson et al. 2008):

$$I_n \text{ (km mol}^{-1}) = \frac{\pi}{3} \frac{N_A}{c^2} d_n \sum_j |\bar{Z}_{n,j}|^2 = \frac{N_A V v_n^2 d_n}{12 c^2} \sum_j f_{n,j} \tag{4}$$

where d_n is the degeneracy of the mode, N_A the Avogadro constant and c the speed of light. For ortho-enstatite, there is only one non-null diagonal element for each mode: f_{11} (for B_{2u} modes), f_{22} (for B_{3u} modes) and f_{33} (for B_{1u} modes).

The ionic contribution to the dielectric tensor was evaluated as the sum of the oscillator strengths. The electronic (high-frequency) component was calculated with the coupled perturbed Kohn–Sham/HF scheme (CPHF/KS) (Born & Huang 1954; Ferrero et al. 2007, 2008a,b, 2009).

The reflectance spectrum $R(v)_j$ is defined in terms of the dielectric function $\epsilon(v)_j$ (Decius & Hexter 1977):

$$R(v)_j = \left| \frac{\sqrt{\epsilon(v)_j - \sin^2(\theta)} - \cos(\theta)}{\sqrt{\epsilon(v)_j - \sin^2(\theta)} + \cos(\theta)} \right|^2, \tag{5}$$

where θ is the incident angle. The complex dielectric function is a diagonal tensor:

$$\epsilon(v)_j = \epsilon_{\infty,j} + \sum_n \frac{f_{n,j} v_n^2}{v_n^2 - v^2 - iv\gamma_n}, \tag{6}$$

where γ_n is the damping factor of mode n.

Semi-empirical γ_n values, derived by fitting the computed reflectance spectrum to the experimental one, were used, as the harmonic model adopted in our quantum mechanical simulation does not provide them.

In the experiment, each band with a good signal-to-noise ratio was interpreted as due to a single oscillator. The corresponding ϵ_∞, f, v and γ values were obtained by fitting equation (5) to the measured reflection spectra, and no deconvolution process was tried to the broad-bands.

Manipulation and visualization of structures were performed with the MOLDRAW program (http://www.moldraw.unito.it) and the Jmol 3D engine (http://jmol.sourceforge.net/). Molecular drawings were rendered with the INKSCAPE-0.46 program (http://www.inkscape.org) using input files prepared with Jmol.

3 EXPERIMENTAL METHODS

The ortho-enstatite sample was synthesized with the top-seeded solution growth (Tanaka & Takei 1997) and flux method (Ito 1975). The original sample was cut into smaller pieces and the surfaces normal to crystalline axes were polished. The final sizes of the samples are of the order of a millimetre and luminous probe light

was required to obtain reflection spectra with good signal-to-noise ratio.

We utilized the IR beamline in the synchrotron radiation facility SPring8 in Japan. An S-polarized beam was used. The grid polarizer was equipped to pick the polarization direction. The probe light beam was from electrons ($E = 8$ GeV) on a 1.4 m arc track with an applied magnetic field of 0.679 498 T. The light beam was collimated and fed to a Michelson-type interferometer (Bruker IFS125 Fourier spectrometer), and then focused to the enstatite sample. The reflected beam from the sample was refocused to a mercury/cadmium/telluride diode or a silicon bolometer for the detection of IR light of larger (>400 cm^{-1}) or smaller (<400 cm^{-1}) wavenumber, respectively. A Ge-coated KBr substrate was used as beamsplitter for wavenumbers larger than 400 cm^{-1}, a Myler film for wavenumbers smaller than 400 cm^{-1}. The spectral range from 2000 to 100 cm^{-1} was measured with resolution between 1 and 0.25 cm^{-1}, depending on the measured wavenumber. Beam incident angle (θ in equation 5) to the sample was $10°$. The polarization direction of probe light was set by the grid polarizer on KRS5 or polyethylen substrates to be aligned with the crystalline axis. The optical path from the synchrotron ring to the final detector was under vacuum conditions so that the measurements were not affected by absorptions of the gases in the air.

The enstatite samples and a gold-coated mirror were mounted on one sample plate. The plate was on a sliding stage and movable in the direction crossing the light beam. The reflection of the gold mirror was taken after the measurement of an enstatite sample and used for normalization. The reflectivity of the gold mirror was assumed to be 100 per cent for the whole spectral region. A pin hole with diameter 1 mm was put in front of the sample stage to regulate beam size and make flux on each sample identical.

A cryocooler was placed on the top of a 200 mm^3 cubic chamber which contains the sample stage. Flexible copper wires were used in connecting the sample plate and the head of the cryocooler. The heating resisters and Si diode temperature sensors were attached to the sample plate to control the sample temperature. The temperature of the sample was set between 300 and 60 K. Peaks, especially at small wavenumbers, become narrower and higher with decreasing temperature, which allows us to identify some of those having small intensity at room temperature. The experimental wavenumbers presented in the following section were collected at a temperature of 60 K.

4 RESULTS AND DISCUSSION

4.1 Structure

The crystal structure of ortho-enstatite (*Pbca* space group, 80 atoms in the unit cell, 10 of which are symmetry independent), shown in Figs 1 and 2, is built up by SiO$_4$ and MgO$_6$ distorted tetrahedra and octahedra, respectively. Two symmetry-independent Si and Mg atoms are present in the unit cell. The two SiO$_4$ tetrahedra are quite similar, whereas large differences characterize the two MgO$_6$ octahedra (the corresponding Mg atoms will be indicated as Mg$_a$ and Mg$_b$).

Three vertices (basal) of the SiO$_4$ tetrahedron define a plane which is nearly parallel to the plane defined by the *b* and *c* lattice vectors; the fourth vertex (apical) is along the axis perpendicular to this plane. Each SiO$_4$ tetrahedron shares two basal vertices with two other tetrahedra to form chains oriented along the *c*-axis. Both these vertices are linked to a Mg$_a$O$_6$ unit. The other basal SiO$_4$ vertex is
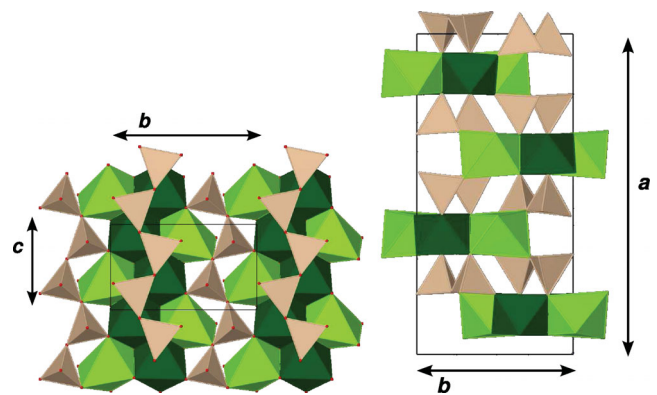

Figure 1. View along the *a*-axis (left) and *c*-axis (right) of ortho-enstatite: SiO$_4$, Mg$_a$O$_6$ and Mg$_b$O$_6$ polyhedra in brown, green and dark green, respectively; the cell shape is indicated in both figures. SiO$_4$ and Mg$_b$O$_6$ single chains are oriented along the *c*-axis. Mg$_a$O$_6$ octahedra are less regular than Mg$_b$O$_6$, see Fig. 2.
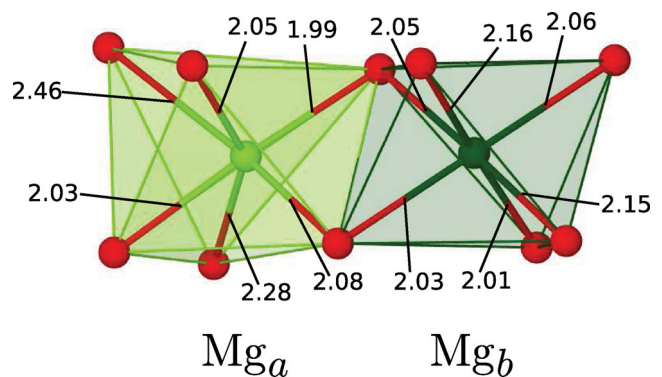
Figure 2. Mg$_a$O$_6$ and Mg$_b$O$_6$ polyhedra. Calculated Mg–O bond lengths (Å) are reported.

linked to a Mg$_a$O$_6$ and a Mg$_b$O$_6$ octahedron. The apical oxygen is shared by two Mg$_b$O$_6$ and one Mg$_a$O$_6$ octahedra.

Mg$_b$O$_6$ octahedra are linked to each other by edge sharing and form a chain superposed to the SiO$_4$ chain along the *c*-axis. Mg$_a$O$_6$ octahedra share three edges with three different Mg$_a$O$_6$ octahedra.

The calculated and experimental (Ohashi 1984; Ghose et al. 1986) equilibrium geometries are compared in Table 1, showing very good

Table 1. Experimental and calculated structure of ortho-enstatite. *a*, *b* and *c* are the cell parameters and *V* is the cell volume. The maximum (max) and minimum (min) Si–O and Mg–O bond distances are reported. Lengths are given in Å and volume is given in Å^3.

	XRD single crystals		Calculated
	Ohashi (1984)	Ghose, Schomaker & McMullan (1986)	This work
a	18.2250	18.2350	18.2433
b	8.8129	8.818	8.8295
c	5.180	5.179	5.1931
V	832.98	832.76	836.50
Mg–O$_{min}$	1.992	1.992	1.9902
Mg–O$_{max}$	2.445	2.447	2.4607
Si–O$_{min}$	1.585	1.588	1.5970
Si–O$_{max}$	1.679	1.678	1.6843

Table 2. Calculated (PBE0) and experimental (60 K) IR active vibrational frequencies (ν, cm^{-1}) and oscillator strengths f (adimensional and multiplied by 10^3) along the *a*-axis (B_{2u}). Experimental f values are significant down to order 0.1. $\Delta\nu$ and Δf are the differences between experimental and calculated quantities. $\sum f$ is the sum of the oscillator strengths and ($\sum|\Delta f|$) the absolute difference between experimental and calculated oscillator strengths; $|\Delta|_{\max}$, $\bar{\Delta}$ and $\overline{|\Delta|}$ are the maximum absolute, the mean and the mean absolute differences, respectively (evaluated with respect to $N = 22$ experimental values). f is in bold face when >100. Oscillator strengths are grouped either when the corresponding calculated frequencies differ ($\delta\nu$) by less than 15 cm^{-1} or when $\delta\nu \leq 30$ cm^{-1} and $f_{\text{calc}} \geq 500$.

	ν_{calc}	ν_{exp}	$\Delta\nu$	f_{calc}		f_{exp}		Δf	
1	87.4	–	–	4.3	4.3	–	–	–	–
2	144.8	–	–	10.7	10.7	–	–	–	–
3	191.3	193.6	2.3	**177.1**	**177.1**	**169.0**	**169.0**	−8.1	−8.1
4	201.6	204.3	2.7	**171.9**	**171.9**	**202.0**	**202.0**	30.1	30.1
5	236.9	–	–	7.1	7.1	–	–	–	–
6	265.6	–	–	1.5	1.5	–	–	–	–
7	287.6	–	–	30.1	} 109.6	–		–	} 15.4
8	296.7	293.3	−3.4	79.5		**125.0**	**125.0**	45.5	
9	305.9	303.2	−2.7	**463.1**	}	**188.0**	}	−275.1	}
10	317.8	317.4	−0.4	**1587.6**	} **2248.2**	**582.0**	} **2100.0**	−1005.6	} −148.2
11	328.7	326.4	−2.3	**197.4**	}	**1330.0**	}	1132.6	}
12	352.6	351.3	−1.3	**192.4**	**192.4**	**292.0**	**292.0**	99.6	99.6
13	377.9	370.5	−7.4	**109.4**	**109.4**	92.2	92.2	−17.2	−17.2
14	413.3	406.0	−7.3	8.3	8.3	20.1	20.1	11.8	11.8
15	430.6	421.3	−9.3	**152.0**	**152.0**	**189.0**	**189.0**	37.0	37.0
16	446.2	436.0	−10.2	81.9	} 164.7	95.7	} 169.9	13.8	} 5.2
17	459.3	448.8	−10.5	82.7		74.2		−8.5	
18	509.2	504.4	−4.8	2.3	2.3	6.4	6.4	4.1	4.1
19	535.7	523.4	−12.3	42.2	42.2	46.4	46.4	4.2	4.2
20	553.6	545.1	−8.5	50.6	50.6	36.9	36.9	−13.7	−13.7
21	570.6	555.9	−14.7	**107.6**	**107.6**	**102.0**	**102.0**	−5.6	−5.6
22	653.1	645.2	−7.9	65.0	65.0	74.8	74.8	9.8	9.8
23	689.2	681.0	−8.2	4.5	4.5	3.6	3.6	−0.9	−0.9
24	868.0	–	–	0.6	0.6	–	–	–	–
25	946.0	–	–	1.8	} 495.1	–	} 524.0		} 28.9
26	950.2	939.5	−10.7	**493.4**		**524.0**		30.6	
27	1026.7	1012.8	−13.9	26.5	26.5	29.1	29.1	2.6	2.6
28	1066.7	1054.6	−12.1	**144.3**	**144.3**	**145.0**	**145.0**	0.7	0.7
29	1170.7	1151.9	−18.8	1.1	1.1	1.6	1.6	0.5	0.5
$\sum f$ ($\sum|\Delta f|$)				4296.9		4329.0		(2757.6)	(443.6)
$|\Delta|_{\max}$			18.8					1132.6	148.2
$\overline{|\Delta|}$			7.8						
$\bar{\Delta}$			−7.4						

agreement (largest deviation: +0.6 per cent on the Si–O$_{\min}$ bond distance; +0.3 per cent on the *c* lattice parameter and +0.5 per cent on the volume). The SiO$_4$ tetrahedra turn out to be very irregular (Si–O bonds range from 1.59 to 1.68 Å).

The most relevant difference between Mg$_b$O$_6$ and Mg$_a$O$_6$ octahedra is in the structural organization (as already discussed, the former build up chains to which the latter are linked at the two sides) and the Mg–O bond distances: Mg$_a$O$_6$ are very distorted octahedra, with Mg–O distances ranging from 1.99 to 2.46 Å, whereas Mg$_b$O$_6$ are more regular, with Mg–O distances ranging from 2.01 to 2.16 Å (see Fig. 2).

4.2 Infrared modes: wavenumbers and intensities

The decomposition of the reducible representation built on the basis of the Cartesian coordinates of the unit cell atoms leads to the following symmetry assignment of the 240 normal modes (D_{2h} point group):

$$\Gamma_{\text{total}} = 30(B_{1u} + B_{2u} + B_{3u} + B_{1g} + B_{2g} + B_{3g} + A_u + A_g). \tag{7}$$

There are 87 IR active modes ($29B_{1u}$, $29B_{2u}$ and $29B_{3u}$; the three frequencies corresponding to pure translations have B_{1u}, B_{2u} and B_{3u} symmetry), 120 Raman active modes ($30B_{1g}$, $30B_{2g}$, $30B_{3g}$ and $30A_g$) and 30 'silent' A_u modes.

In the present study we focus our attention on the 87 IR active modes and compare the results obtained with simulation (0 K) and experiment (60 K), where 65 peaks are clearly identified.

The 22 missing peaks in general correspond to modes with a low calculated intensity (oscillator strength, f, smaller than 10, on a scale that reaches $f = 1600$ – mode 10 in Table 2) or to modes very close to intense peaks. Note that f values are multiplied by 10^3 from now on, in order to simplify the notation.

Tables 2, 3 and 4 document the quite good agreement between calculated and experimental wavenumbers. In order to perform a systematic comparison, and considering that experimental

Table 3. Calculated and experimental (60 K) IR active vibrational frequencies and oscillator strengths along the *b*-axis (B_{3u}). Symbols and units as in Table 2. Statistical indices evaluated with respect to $N = 22$ experimental values.

	ν_{calc}	ν_{exp}	$\Delta\nu$	f_{calc}		f_{exp}		Δf	
1	114.6	–	–	9.9	9.9	–	–	–	–
2	200.6	–	–	15.3	15.3	–	–	–	–
3	223.0	220.5	−2.5	**120.2**		**310.0**		189.8	
4	223.1	224.1	1.0	**1291.2**	**1584.7**	**1020.0**	**1518.0**	−271.2	−66.7
5	242.6	241.9	−0.7	**173.3**		**188.0**		14.7	
6	274.4	271.2	−3.2	**435.1**	**435.1**	**514.0**	**514.0**	78.9	78.9
7	296.6	295.4	−1.2	94.3	94.3	93.9	93.9	−0.4	−0.4
8	338.5	336.2	−2.3	33.9		22.4		−11.5	
9	351.3	–	–	10.2	**530.2**	–	**634.4**	–	104.2
10	358.3	349.9	−8.4	**486.1**		**612.0**		125.9	
11	382.6	379.3	−3.3	35.0	35.0	22.1	22.1	−12.9	−12.9
12	407.0	397.3	−9.7	12.9		3.6		−9.2	
13	419.4	413.5	−5.9	28.2	41.1	21.8	25.4	−6.4	−15.6
14	440.5	433.9	−6.6	1.6	1.6	4.6	4.6	3.0	3.0
15	471.4	463.0	−8.4	**339.1**		**215.0**		−124.1	
16	481.9	475.3	−6.6	**872.9**	**1220.7**	**919.0**	**1134.0**	46.1	−86.7
17	487.7	–	–	8.7		–		–	
18	494.9	–	–	0.5	0.5	–	–	–	–
19	519.4	–	–	0.8	0.8	–	–	–	–
20	559.4	549.5	−9.9	18.0	18.0	20.2	20.2	2.2	2.2
21	577.5	568.1	−9.4	23.5	23.5	25.0	25.0	1.5	1.5
22	736.1	724.7	−11.4	42.0	42.0	47.3	47.3	5.3	5.3
23	756.8	745.6	−11.2	6.9	6.9	11.2	11.2	4.2	4.2
24	902.1	889.6	−12.5	**239.8**	**239.8**	**258.0**	**258.0**	18.2	18.2
25	923.6	–	–	12.2	39.8	–	27.0	–	−12.8
26	929.2	919.3	−9.9	27.6		27.0		−0.6	
27	1026.2	1013.3	−12.9	44.0	94.2	46.0	99.7	2.0	5.5
28	1034.9	1021.1	−13.8	50.2		53.7		3.5	
29	1086.0	1072.4	−13.6	**191.1**	**191.1**	**198.0**	**198.0**	6.9	6.9
$\sum f$ ($\sum|\Delta f|$)				4624.5		4632.8		(938.5)	(425.0)
$|\Delta|_{max}$			13.8					271.2	104.2
$\overline{|\Delta|}$			7.5						
$\bar{\Delta}$			−7.3						

oscillator strengths are affected by a larger uncertainty with respect to the experimental frequencies, data for a given symmetry were ordered on the basis of the least difference between experimental and calculated vibrational frequencies. The fact that this difference is nearly systematic confirms that this is a reasonable method. However, there are some exceptions, as lines 25–26 of Table 2 (the smallest difference is between the experimental frequency of line 26 and the calculated frequency of line 25, but it is evident from *f* that it corresponds to the calculated frequency of line 26) and 9–10 of Table 3 (similar comment). The case of lines 25–26 in Table 3 can be interpreted in a similar way, even if there is not such clear evidence ($f_{calc} = 12$ versus $f_{exp} = 27$ with respect to $f_{calc} = 2$ versus $f_{exp} = 524$ in Table 2). This point, together with the fact that the disagreement between ν_{exp} and ν_{calc} in the region >900 cm^{-1} of the spectrum is always larger than 10 cm^{-1}, suggests associating the experimental value with the calculated frequency on line 26.

The mean absolute $\overline{|\Delta|}$, the mean $\bar{\Delta}$ and the maximum absolute difference $|\Delta_{max}|$ are reported in the tables. $\overline{|\Delta|}$ values are 7.8, 7.5 and 7.4 cm^{-1} for the B_{2u}, B_{3u} and B_{1u} sets, respectively, and the corresponding $\bar{\Delta}$ values are −7.4, −7.3 and −6.7 cm^{-1} for the three cases. The very close $\overline{|\Delta|}$ and $\bar{\Delta}$ values indicate that there is a systematic overestimation of the calculated frequencies with respect to the experimental ones. This is a well-known feature of PBE0 functional, which provides accurate geometries (Demichelis et al. 2010a,b) and a slight overestimation of the calculated vibrational frequencies. $|\Delta_{max}|$ never exceeds 20 cm^{-1}.

If the calculated frequencies are shifted by $\bar{\Delta}$, the mean absolute difference, $|\bar{\delta}| = \frac{\sum_i^{n_i} |\nu_i^{exp} - \nu_i^{calc} - \bar{\Delta}|}{n_i}$, becomes extremely small: 4.4, 3.7 and 5.8 cm^{-1} in the three Cartesian directions, respectively.

As the experiments are performed at 60 K, and the simulation refers to 0 K, a small fraction of the discrepancy might be due to temperature effects.

The 22 peaks not observed in the experimental determination are equally distributed along the three directions (7, 7 and 8 in B_{2u}, B_{3u} and B_{1u}, respectively). Most of them (1, 2, 5, 6 and 24 in Table 2; 1, 2, 9, 17, 18 and 19 in Table 3; 3, 5, 9, 12 and 15 in Table 4, for a total of 16) have very weak calculated oscillator strength, *f* ($f < 16$, one-hundredth of the largest one with $f \simeq 1600$, see mode 10 in Table 2). In particular, due to the decreasing brilliance of the synchrotron radiation with decreasing wavenumber, the sensitivity of the instrument is lower in the 100–200 cm^{-1} region and weak peaks, as numbers 1 and 2 in Tables 2 and 3, were not detected. Also, the damping factors are usually

Table 4. Calculated and experimental (60 K) IR active vibrational frequencies and oscillator strengths along the *c*-axis (B_{1u}). Symbols and units as in Table 2. Statistical indices evaluated with respect to $N = 21$ experimental values.

	ν_{calc}	ν_{exp}	$\Delta\nu$	f_{calc}		f_{exp}		Δf	
1	137.1	139.7	2.6	73.9	⎫ 130.0	68.8	⎫ 124.8	−5.1	⎫ −5.2
2	147.1	147.2	0.1	56.1	⎭	56.0	⎭	−0.1	⎭
3	179.2	–	–	5.8	5.8	–	–	–	–
4	196.2	196.5	0.3	61.6	61.6	70.8	70.8	9.2	9.2
5	229.2	–	–	3.7	⎫ 154.2	–	⎫ 181.0	–	⎫ 26.8
6	238.2	237.6	−0.6	**150.5**	⎭	**181.0**	⎭	30.5	⎭
7	284.9	282.3	−2.6	24.0	24.0	26.9	26.9	2.9	2.9
8	300.1	305.0	4.9	0.7	⎫ 12.2	5.1	⎫ 5.1	−4.4	⎫ −7.1
9	313.2	–	–	11.5	⎭	–	⎭	–	⎭
10	331.3	328.4	−2.9	18.4	18.4	29.0	29.0	10.6	10.6
11	354.7	353.9	−0.8	0.1	⎫ 12.9	29.8	⎫ 29.8	−29.7	⎫ 16.9
12	358.0	–	–	12.8	⎭	–	⎭	–	⎭
13	394.6	–	–	36.8	⎫ 580.0	–	⎫ 555.0	–	⎫ −25.0
14	413.9	407.7	−6.2	**542.2**	⎬	**555.0**	⎬	12.8	⎬
15	439.2	–	–	1.1	⎭	–	⎭	–	⎭
16	464.0	462.8	−1.2	**351.7**	⎫ 574.1	552.0	⎫ 552.0	200.3	⎫ −22.1
17	471.4	–	–	**183.4**	⎭	–	⎭	–	⎭
18	486.4	–	–	39.0	⎫ 1317.2	–	⎫ 1320.0	–	⎫ 2.8
19	510.7	504.1	−6.6	**1278.2**	⎭	**1320.0**	⎭	41.8	⎭
20	547.5	537.4	−10.2	**155.1**	**155.1**	**141.0**	**141.0**	−14.1	−14.1
21	585.4	570.0	−15.3	39.0	39.0	22.0	22.0	−17.0	−17.0
22	662.3	655.5	−6.8	19.9	19.9	20.1	20.1	0.2	0.2
23	705.5	695.3	−10.2	45.1	45.1	43.7	43.7	−1.4	−1.4
24	868.0	850.4	−17.6	**326.6**	**326.6**	**346.0**	**346.0**	19.4	19.4
25	940.9	928.0	−12.9	**261.8**	**261.8**	**280.0**	**280.0**	18.2	18.2
26	988.8	977.5	−11.3	15.0	15.0	12.4	12.4	−2.6	−2.6
27	1022.1	1008.1	−14.1	6.2	6.2	8.5	8.5	2.3	2.3
28	1052.6	1042.5	−10.1	10.3	10.3	8.2	8.2	−2.1	−2.1
29	1152.5	1133.5	−19.0	12.0	12.0	14.9	14.9	2.9	2.9
$\sum f$ $(\sum\lvert\Delta f\rvert)$				3736.7		3791.3		(427.6)	(208.8)
$\lvert\Delta\rvert_{max}$			19.0					200.3	26.8
$\overline{\lvert\Delta\rvert}$			7.4						
$\bar{\Delta}$			−6.7						

large in this region, making peaks flat and broad, and so difficult to detect.

Four missing peaks (numbers 7, 25, 13 and 18 in the three directions, respectively) are characterized by slightly larger calculated oscillator strength ($f < 40$). However, they are close ($\pm 30\,cm^{-1}$) to intense peaks ($f > 100$), which overlap and hide them.

Similarly, the couples of mode numbers 26 ($f = 493$) and 25 ($f = 1.8$) in Table 2, and 17 ($f = 183$) and 16 ($f = 352$) in Table 4, are experimentally detected as single peaks, as a consequence of extremely close frequencies (the calculated difference is smaller than $5\,cm^{-1}$).

The sum of the oscillator strength, $\sum f$ (i.e. the ionic contribution to the dielectric tensor), given in the same tables, permits us to appreciate the extremely good agreement between experimental and calculated data: 4329 versus 4297 (B_{2u}), 4633 versus 4624 (B_{3u}) and 3791 versus 3737 (B_{1u}), respectively (difference <1.5 per cent). However, the sum of the absolute differences (see $\sum\lvert\Delta f\rvert$ in Tables 2, 3 and 4) is quite large (2758, 939 and 428). A rapid analysis shows that large differences appear for most of the modes with very close frequencies (see lines grouped in columns 6, 8 and 10 of Tables 2, 3 and 4). As anticipated in a previous paragraph, the one-to-one correspondence between calculated and experimental modes having the same symmetry is to a large amount arbitrary in these cases. For this reason, f belonging to two (or more) frequencies with $\Delta\nu \le 15\,cm^{-1}$, or with $\Delta\nu \le 30\,cm^{-1}$ and $f_{calc} \ge 500$, were grouped before comparison. Moreover, problems affecting the assignment of the bands in the experimental spectrum when modes are close in frequency are evident. For example, the differences between experimental and calculated f for modes 9, 10 and 11 in Table 2 are very large ($-275, -1006, +1133$), but they reduce overall to -148 after grouping.

This strategy and a careful attribution of the modes which appear as a single peak in the experimental spectrum reduce $\sum\lvert\Delta f\rvert$ to 443 (10.2 per cent), 425 (9.2 per cent) and 209 (5.5 per cent), as shown in Tables 2, 3 and 4. The agreement between experimental and calculated f is then excellent.

An overall comparison between experimental and simulated IR data can be obtained by comparing the reflection spectra. The experimental ν_n, f_n and γ_n values are obtained from the primary yield of the experiment by best fit (see equation 5). The simulated spectrum is obtained by using ab initio ν_n and f_n, and semi-empirical γ_n as described in Section 2, as our harmonic models are unable to provide them.
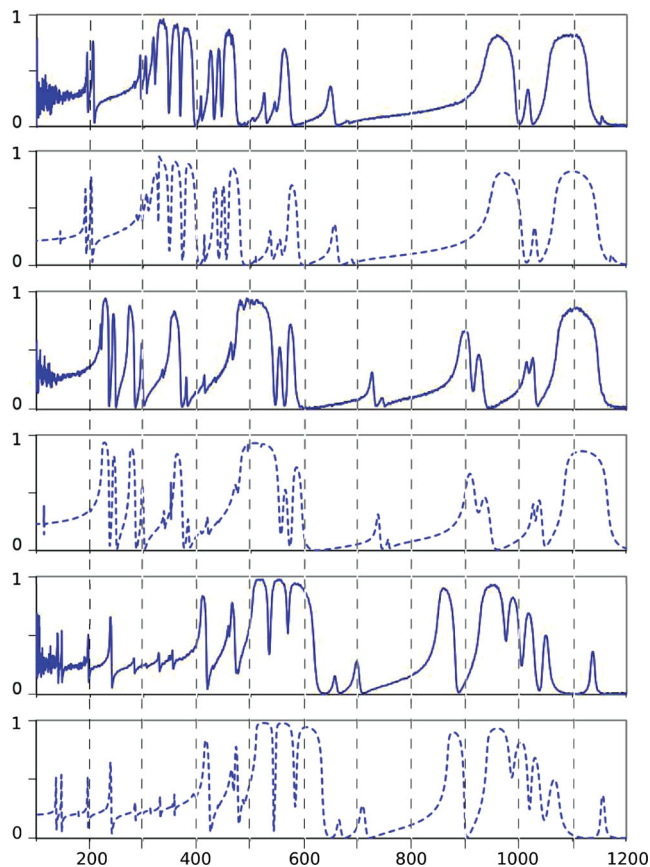
Figure 3. Measured (line, 60 K) and simulated (dashed line) reflection spectra of ortho-enstatite along the x (a, b), y (c, d) and z (e, f) directions. Frequencies are given in cm^{-1} and the oscillator strengths are normalized to 1. Note that ab initio ν_n and f_n and experimental γ_n are used to produce the simulated plot.

Fig. 3 shows the extremely good agreement between experiment and theory. Panels (a), (c) and (e) provide the experimental spectrum as recorded. Panels (b), (d) and (f) are obtained by computing the spectrum through equation (5).

4.3 Dielectric properties

The diagonal components of the electronic dielectric tensor (ϵ_∞ in Table 5) obtained by using the CPKS (Born & Huang 1954; Ferrero et al. 2007, 2008a,b, 2009) scheme are 2.544, 2.526 and 2.555, to be compared to the experimental values at 2.69 (+5.4 per cent), 2.66 (+5.0 per cent) and 2.76 (+7.4 per cent).

The agreement for the ionic contribution, evaluated as the sum of the oscillator strengths, is even better: calculated and experimental

values are 4.297 versus 4.329 (+0.7 per cent), 4.624 versus 4.633 (+0.2 per cent) and 3.737 versus 3.791 (+1.4 per cent), respectively.

Overall, the calculated components of the static dielectric tensor (ϵ_0), obtained by the sum of the electronic and ionic contributions, is underestimated by 2.5, 2.0 and 3.9 per cent with respect to experiment.

As a cross-check on the validity of the data provided here, it is interesting to compare ϵ_∞ to the index of refraction in visible. Experimental ϵ_∞ versus the refraction indices in visible [from Handbook of Mineralogy (UofA), http://webmineral.com/data/Enstatite.shtml] are 2.69 versus 2.72–2.78, 2.66 versus 2.73–2.79 and 2.76 versus 2.74–2.82 for the three Cartesian directions, respectively. It is reasonable that ϵ_∞ (derived using the wavelength longer than 2 μm) are smaller than those obtained at visible wavelength, because the dielectric function decreases with increasing wavelength from visible to near-IR as no vibrational mode falls in this region.

5 CONCLUSIONS

The IR spectrum of ortho-enstatite was measured with IR beamline synchrotron radiation and calculated with ab initio techniques. The comparison involves a very large number of wavenumbers and oscillator strengths (65), showing that

(a) when high-quality experimental and calculated data are available, very good agreement can be achieved, and a very detailed description of vibrational properties (wavenumbers and oscillator strengths) can be provided;

(b) factors that can reduce the accuracy of experiment (quality of the sample, experimental setup and accuracy of the band assignment) or simulation (approximation of the Hamiltonian, finite basis set) are different, and a cross-comparison can eliminate (or 'filter') anomalous behaviours (for example, a systematic and small overestimation – around 8 cm^{-1} – of calculated with respect to experimental vibrational frequencies is obtained, with a quite reduced dispersion; once the calculated frequencies are corrected by 8 cm^{-1}, differences become very small);

(c) simulation is also helpful in the interpretation of the experimental spectrum, as it allows a more detailed analysis of the nature of the modes and can confirm that a fraction of symmetry allowed modes do not appear in the experimental spectrum due to their low intensity or to very close frequency;

(d) the combined application of these two tools permits us to obtain the full set of IR active modes, including their intensities, which can be used as a reference for comparison with unknown samples.

To the authors' knowledge this paper represents one of the most complete and accurate comparisons of experimental and calculated vibrational results extended to such a large set of data.

Table 5. Calculated and experimental static dielectric tensor (ϵ_0) and its components: the electronic high frequency (ϵ_∞) and the ionic one, evaluated as the sum of the oscillator strengths ($\sum f$). Δ (per cent) $= \frac{\text{exp}-\text{calc}}{\text{exp}} \times 100$.

| | ϵ_0 | | | ϵ_∞ | | | $\sum f$ | | |
	calc	exp	Δ (per cent)	calc	exp	Δ (per cent)	calc	exp	Δ (per cent)
xx	6.841	7.019	+2.5	2.544	2.69	+5.4	4.297	4.329	+0.7
yy	7.150	7.293	+2.0	2.526	2.66	+5.0	4.624	4.633	+0.2
zz	6.292	6.551	+3.9	2.555	2.76	+7.4	3.737	3.791	+1.4

REFERENCES

Adamo C., Barone V., 1999, J. Chemical Phys., 110, 6158

Balan E., Blanchard M., Hochepied J. F., Lazzeri M., 2008, Phys. Chemistry Minerals, 35, 279

Baranek P., Zicovich-Wilson C., Roetti C., Orlando R., Dovesi R., 2001, Phys. Rev. B, 64, 125102

Born M., Huang K., 1954, Dynamical Theory of Crystal Lattices. Oxford Univ. Press, Oxford

Broyden C. G., 1970, J. Inst. Math. Applications, 6, 76

Civalleri B., D'Arco P., Orlando R., Saunders V. R., Dovesi R., 2001, Chemical Phys. Lett., 348, 131

Decius J. C., Hexter R. M., 1977, Molecular Vibrations in Crystals. McGraw-Hill, New York

Demichelis R., Civalleri B., Ferrabone M., Dovesi R., 2010a, Int. J. Quantum Chemistry, 110, 406

Demichelis R., Civalleri B., D'Arco P., Dovesi R., 2010b, Int. J. Quantum Chemistry, 110, 2260

Doll K., 2001, Comput. Phys. Commun., 137, 74

Doll K., Harrison N. M., Saunders V. R., 2001, Int. J. Quantum Chemistry, 82, 1

Dovesi R. et al., 2009, CRYSTAL 2009 User's Manual. Univ. degli Studi di Torino, Torino

Ferrero M., Rérat M., Orlando R., Dovesi R., 2007, in Simos T. E., Maroulis G., eds, AIP Conf. Proc. Vol. 963, Computation in Modern Science and Engineering. Am. Inst. Phys., New York, p. 1199

Ferrero M., Rérat M., Orlando R., Dovesi R., 2008a, J. Chemical Phys., 128, 014110

Ferrero M., Rérat M., Orlando R., Dovesi R., 2008b, J. Comput. Chemistry, 29, 1450

Ferrero M., Civalleri B., Rérat M., Orlando R., Dovesi R., 2009, J. Chemical Phys., 131, 214704

Fletcher R., 1970, Comput. J., 13, 317

Ghose S., Schomaker V., McMullan R. K., 1986, Z. Kristallographie, 176, 159

Goldfarb D., 1970, Math. Comput., 24, 23

Ito J., 1975, Geophys. Res. Lett., 12, 533

Noël Y., Zicovich-Wilson C., Civalleri B., D'Arco P., Dovesi R., 2002, Phys. Rev. B, 65, 014111

Noël Y., Catti M., D'Arco P., Dovesi R., 2006, Phys. Chemistry Minerals, 33, 383

Ohashi Y., 1984, Phys. Chemistry Minerals, 10, 217

Olofsson J. et al., 2009, A&A, 507, 327

Pascale F., Zicovich-Wilson C. M., Gejo F. L., Civalleri B., Orlando R., Dovesi R., 2004, J. Comput. Chemistry, 25, 888

Pisani C., Dovesi R., Roetti C., Causà M., Orlando R., Casassa S., Saunders V. R., 2000, Int. J. Quantum Chemistry, 77, 1032

Shanno D. F., 1970, Math. Comput., 24, 647

Spoon H. W. W. et al., 2006, ApJ, 638, 759

Tanaka T., Takei H., 1997, J. Crystal Growth, 180, 206

Wooden D. H., Woodward C. E., Harker D. E., 2004, ApJ, 612, L77

Zicovich-Wilson C., Dovesi R., Saunders V. R., 2001, J. Chemical Phys., 115, 9708

Zicovich-Wilson C., Bert A., Roetti C., Dovesi R., Saunders V. R., 2002, J. Chemical Phys., 116, 1120

Zicovich-Wilson C. M., Torres F. J., Pascale F., Valenzano L., Orlando R., Dovesi R., 2008, J. Comput. Chemistry, 29, 2268

This paper has been typeset from a T$_{\rm E}$X/L$^{\rm A}$T$_{\rm E}$X file prepared by the author.